Journal of Materials Chemistry A

ROYAL SOCIETY OF CHEMISTRY

PAPER

View Article Online
View Journal | View Issue

Cite this: J. Mater. Chem. A, 2022, 10, 5971

Zinc/graphitic carbon nitride co-mediated dual-template synthesis of densely populated Fe–N_x-embedded 2D carbon nanosheets towards oxygen reduction reactions for Zn–air batteries†

Xiao-Fei Gong,[a] Yun-Long Zhang,[a] Lei Zhao, *[a] Yun-Kun Dai,[a] Jia-Jun Cai,[a] Bing Liu,[a] Pan Guo,[a] Qing-Yan Zhou,[a] Ichizo Yagi [c] and Zhen-Bo Wang *[ab]

Atomically dispersed Fe–N–C catalysts have been extensively deemed as appealing substitutes for Pt-series catalysts towards oxygen reduction reactions (ORRs). Nevertheless, most reported Fe–N–C materials suffer from inefficient Fe-based nanoparticles and low-density Fe–N_x sites. Herein, a Zn/g-C_3N_4-mediated dual-template strategy was employed to synthesize densely populated atomic Fe–N_x center-embedded N-doped carbon nanosheets (SAs-Fe/N-CNSs) with adjustable porous structures by the simple pyrolysis of D-glucosamine/FeZn/g-C_3N_4 complexes. g-C_3N_4 works as a structure-guiding 2D template and offers abundant coordination-N trapping sites for anchoring Fe atoms, simultaneously. $ZnCl_2$ serves as a self-sacrificial template creating a hierarchical porous structure by its volatilization as well as hinders the agglomeration of Fe atoms by spatial segregation during pyrolysis. Due to the high-density atomic Fe–N_x moieties, unique 2D structure, hierarchical porosity, and large surface area, the optimal SAs-Fe/N-CNS catalyst exhibits satisfying ORR performance including excellent activity ($E_{1/2}$ = 0.91 V) and desirable durability, surpassing the Pt/C catalyst. Additionally, the superb performance of SAs-Fe/N-CNS-based Zn–air batteries with a maximum power density of 157.03 mW cm^{-2} verifies their promising application in practical electrochemical systems.

Received 17th September 2021
Accepted 19th October 2021

DOI: 10.1039/d1ta08007e

rsc.li/materials-a

Introduction

With the growing depletion of fossil fuel and increasing emission from internal combustion engines, energy dilemma and environmental pollution issues have become a serious concern,[1–3] which can be relieved *via* developing clean and efficient energy conversion and storage devices, such as metal-air batteries and fuel cells.[4–7] However, their practically commercial implementation is primarily obstructed by the cathodic oxygen reduction reaction (ORR) with sluggish kinetics,[8–11] demanding efficient but scarce Pt-based catalysts.[12–15]

At present, carbon-based heteroatom-doped non-precious metal catalysts (NPMCs) have been generally considered to be potential substitutes for Pt-series catalysts towards ORRs, based on their merits of desirable conductivities, large surface area, favorable durability together with tunable composition and morphology.[16–19] Among these NPMCs, Fe–N–C catalysts with extremely high activities, abundant resources, and excellent anti-poison ability are expected to deliver the most satisfactory ORR performance, owing to their efficient Fe–N_x active sites with moderate M–O_2 interactions.[20–22] Nevertheless, a great amount of reported Fe–N–C catalysts might suffer from inhomogeneous morphology and structure with massive low-active Fe-based particles, blocking the full access to active sites and reducing the mass activities for catalysts.[23–25] Towards this end, the atomically dispersed Fe–N–C catalysts are becoming up-rising stars, by virtues of their unique single-atom characteristics with the maximum atom utilization, unsaturated single sites, ideal Fe–N_x configuration, and plentiful active site exposure.[26–28] Despite substantial research on single-atom Fe–N–C materials, further increasing the atomic Fe loading is universally deemed as the bottleneck for extremely efficient Fe–N–C series catalysts, owing to the migration and agglomeration tendency of monatomic Fe moieties driven by their high surface energy.[29,30] Concerning this issue, rationally designing the morphologies and nanostructures of carbon-based materials is vital for constructing high-loading single-atom Fe–N–C catalysts.[31–34]

Well-defined 2D carbon materials have been extensively explored to be appealing catalyst candidates because of their

[a]MIIT Key Laboratory of Critical Materials Technology for New Energy Conversion and Storage, State Key Lab of Urban Water Resource and Environment, School of Chemistry and Chemical Engineering, Harbin Institute of Technology, Harbin, 150001, China. E-mail: leizhao@hit.edu.cn; wangzhb@hit.edu.cn

[b]College of Materials Science and Engineering, Shenzhen University, Shenzhen 518071, Guangdong, China

[c]Faculty of Environmental Earth Science, Graduate School of Environmental Science, Hokkaido University, N10W5, Kita-ku, Sapporo, 060-0810, Japan

† Electronic supplementary information (ESI) available. See DOI: 10.1039/d1ta08007e

large surface area, splendid conductivity, and excellent electronic structure, which can provide expedite mass transfer, sufficient reaction boundary surface together with massive accessible active sites.[35–38] Various approaches including chemical vapor deposition (CVD), mechanical exfoliation as well as electrostatic self-assembly have been adopted to fabricate 2D carbon materials.[39–42] However, the lack of scalable and environment-benign synthetic techniques has severely restricted the widespread application of such unique materials.[43–45] Apart from that, it is highly desirable and challenging to optimize the 2D structures with a higher density of active moieties and favorable hierarchically porous structures for enhanced catalytic performance.[46–48] A multiple-template strategy stands out for its attractive features including the construction of specific morphology, tailoring of hierarchically porous configurations and increase in catalytic active sites.[49–52]

Herein, a facile and versatile Zn/g-C_3N_4-mediated dual-template synthesis method was developed to prepare 2D single-atom-dispersed Fe/N-doped carbon nanosheet (SAs-Fe/N-CNSs) catalysts with dense Fe–N_x sites and hierarchical porosity *via* simply pyrolyzing the D-glucosamine/FeZn/g-C_3N_4 precursors. g-C_3N_4 not only serves as a 2D template, but also offers coordination-N anchoring sites to strengthen the Fe atom-support interaction and avoid the migration of Fe atoms during pyrolysis.[53] Meanwhile, D-glucosamine hydrochloride contributes to inheriting the 2D structure accompanied by the decomposition of the g-C_3N_4 template during pyrolysis.[54,55] Notably, $ZnCl_2$ as a secondary template would also be anchored onto 2D g-C_3N_4 and spatially separate the isolated Fe atoms, inhibiting the Fe atoms from agglomeration to form clusters and nanoparticles. Besides, $ZnCl_2$ can be completely evaporated during pyrolysis, producing abundant micro/mesopores and unsaturated defect sites, which can prevent the porous structure from collapse, offer favorable electron/mass transportation, and provide numerous accessible active sites.[56–58] Benefitting from the dual-template strategy, densely efficient Fe–N_x moieties with atomic dispersion and hierarchical porous system were gained for SAs-Fe/N-CNSs catalysts, which can multiply the accessible active sites and expedite the reactant/product transfer for catalyzing oxygen reduction. Finally, the target SAs-Fe/N-CNS catalyst delivers favorable activity ($E_{1/2}$ = 0.91 V) and enhances the durability for ORRs, surpassing those of Pt/C ($E_{1/2}$ = 0.896 V) and most reported Fe–N–C catalysts. When employed as catalysts in the cathode of Zn–air batteries, the superior performance of SAs-Fe/N-CNSs compared with Pt/C manifests the practical application perspective of our prepared catalyst. Moreover, the high-temperature decomposition of the $ZnCl_2$/g-C_3N_4 template can leave out the complex template removal process that might require poisonous and environmentally harmful ingredients, testifying the applicability of this synthesis strategy in the green and clean energy field.

Results and discussion

The 2D single-atom Fe/N-doped carbon nanosheet (SAs-Fe/N-CNSs) catalysts with high-density Fe–N_x sites and hierarchical porosities were synthesized *via* a facile Zn/g-C_3N_4-mediated dual-template approach, as outlined in Fig. 1a. First, the g-C_3N_4 template prepared by the pyrolysis of melamine was dispersed in deionized water along with D-glucosamine hydrochloride, $FeSO_4 \cdot 7H_2O$, and $ZnCl_2$. Afterwards, this mixture was sonicated for 24 h to obtain a uniform suspension, wherein Fe and Zn ions were coordinated with glucosamine and uniformly anchored onto the g-C_3N_4 nanosheets. After drying at 60 °C overnight, the obtained light yellow powder was pyrolyzed in an Ar atmosphere. During carbonization, the 2D g-C_3N_4 template was decomposed gradually while glucosamine was carbonized and a 2D structure was formed *in situ*. Remarkably, with the volatilization of $ZnCl_2$ under high-temperature conditions, abundant pores and defects were formed within the catalysts, conducing to massively exposed active sites and expedient reactant/product transportation. Ultimately, the SAs-Fe/N-CNSs catalyst was acquired *via* pickling followed by the secondary pyrolysis. For comparison, NPs-Fe/N-CNSs, N-CNSs, and bulk-Fe/N–C were synthesized by a similar preparation process to SAs-Fe/N-CNSs except the acid leaching process, the Fe salt addition, and the g-C_3N_4 addition, respectively. Meanwhile, a series of SAs-Fe/N-CNSs-*x* materials were acquired *via* regulating the molar ratio (*x*) for Zn salt to Fe salt (Zn/Fe, $x = 0$, 1, 2, and 4) by a similar preparation process. Notably, the SAs-Fe/N-CNSs-2 material is denoted as SAs-Fe/N-CNSs in the above discussion.

Scanning electron microscopy (SEM) and transmission electron microscopy (TEM) measurements were first introduced for observing the nanostructure and morphology of these synthesized samples. As presented in Fig. S1,† the obvious 2D nanosheet structure containing plenty of pleated layers was acquired in SAs-Fe/N-CNSs, inheriting the morphology of the g-C_3N_4 template (Fig. S2†). By contrast, SAs-Fe/N-CNSs-0, SAs-Fe/N-CNSs-1, SAs-Fe/N-CNSs-4, N-CNSs, and NPs-Fe/N-CNSs exhibited similar 2D structures (Fig. S3 and S4†), while bulk-Fe/N–C without the addition of g-C_3N_4 displayed an agglomerated bulk morphology (Fig. S5†), demonstrating the indispensability of g-C_3N_4 for forming the 2D structure. Afterwards, the TEM image reveals that a thin sheet-like morphology without visible Fe-related aggregations was observed in SAs-Fe/N-CNSs, beneficial for large surface area and favorable porosity (Fig. 1b). The absence of lattice fringes related to Fe-based species was further demonstrated by the HRTEM results of SAs-Fe/N-CNSs (Fig. 1c), where merely flexural graphene layers with disordered defects were detected. Moreover, the inexistence of Fe-based species was verified through X-ray diffraction (XRD) results. Compared to the distinct Fe and Fe_3C diffraction peaks in NPs-Fe/N-CNSs, nothing but two broad diffraction peaks of ~26° and ~44° corresponding to the (002) and (101) planes in graphitic carbon respectively were detected among SAs-Fe/N-CNSs (Fig. 2a), suggesting the complete elimination or the extremely low content of Fe-containing crystalline species for SAs-Fe/N-CNSs.[59] Moreover, the selected area electron diffraction (SAED) analysis manifested the amorphous carbon structure and poor crystalline of the SAs-Fe/N-CNS material (Fig. 1d). Furthermore, aberration-corrected high-angle annular dark-field scanning transmission electron microscopy (AC HAADF-STEM) analysis demonstrated that only plentiful bright

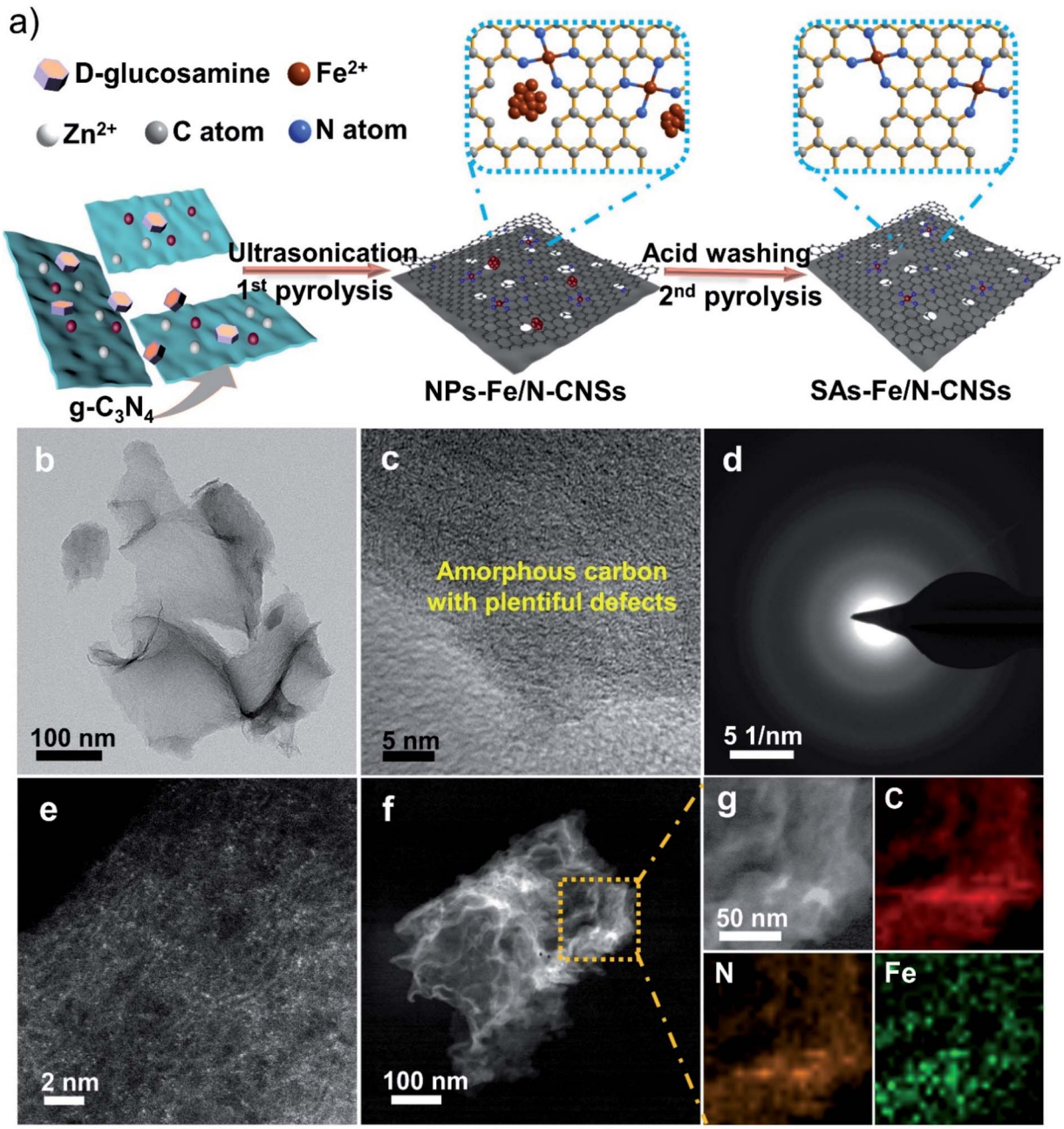

Fig. 1 (a) Schematic of the preparation procedure for SAs-Fe/N-CNSs. (b) TEM, (c) HRTEM, (d) SAED and (e) AC HAADF-STEM images of SAs-Fe/N-CNSs. (f) HAADF-STEM and (g) the relevant C, N and Fe elemental mapping images of SAs-Fe/N-CNSs.

dots relevant to single Fe atoms were evenly scattered all around the SAs-Fe/N-CNSs (Fig. 1e). Additionally, the HAADF-STEM together with its relevant element mapping result verified that the Fe, C, and N elements were homogeneously dispersed in SAs-Fe/N-CNSs without large Fe-related particles (Fig. 1f and g). According to the above-mentioned evidence, it could be inferred that Fe species were evenly embedded within the carbon matrix as a single-atom state and coordinated with the surrounding N atoms (*i.e.* Fe–N_x moieties), which can be further verified by the following X-ray photoelectron spectroscopy (XPS) and X-ray absorption fine structure (XAFS) analyses.

The intensive exploration of the surface chemical composition and electronic configuration of SAs-Fe/N-CNSs and contrastive materials was performed by X-ray photoelectron spectroscopy (XPS) test. As expected, elements containing C, N, Fe, and O were detected in the survey spectra of SAs-Fe/N-CNSs (N: 5.78 at%, Fe: 0.24 at%, C: 84.86 at%, and O: 9.12 at%) and other contrastive samples, except that only C, N, and O elements were detectable in N-CNSs (Fig. S6 and Table S1†). To demonstrate the effect of $ZnCl_2$ on the density of Fe–N_x species, the high-resolution N 1s and Fe 2p spectra of these SAs-Fe/N-CNS materials were investigated. Fig. 2b and S7† reveal that the

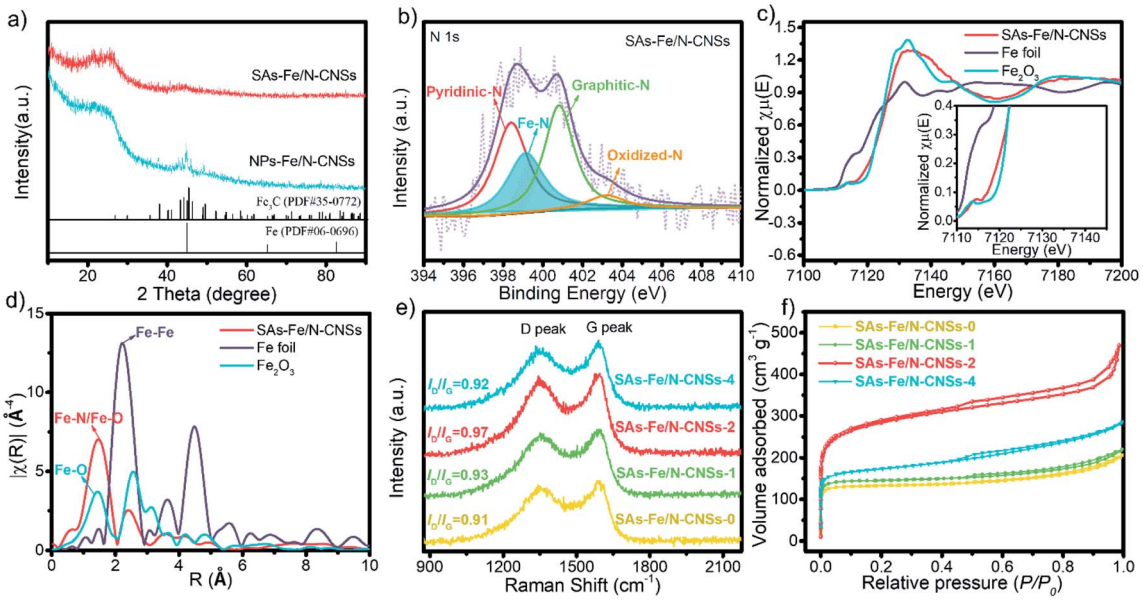

Fig. 2 (a) XRD patterns of SAs-Fe/N-CNSs together with NPs-Fe/N-CNSs. (b) High-resolution N 1s spectra of SAs-Fe/N-CNSs. (c) XANES and (d) EXAFS spectra including SAs-Fe/N-CNSs, Fe foil, and Fe_2O_3. (e) Raman spectra and (f) N_2 adsorption and desorption isotherms including SAs-Fe/N-CNSs-0, SAs-Fe/N-CNSs-1, SAs-Fe/N-CNSs-2, and SAs-Fe/N-CNSs-4, respectively.

high-resolution N 1s spectra of SAs-Fe/N-CNSs-*x* samples are deconvoluted into pyridinic-N (~398.4 eV), Fe–N (~399.2 eV), graphitic-N (~401.1 eV), and oxidized-N (~403.2 eV).[60,61] Notably, SAs–Fe/N-CNSs-2 possesses the highest Fe–N proportion among the SAs-Fe/N-CNSs-*x* catalysts, revealing that an appropriate amount of $ZnCl_2$ is helpful to improve the density of Fe–N_x moieties (Fig. S7c†). Besides, the pyridinic-N and graphitic-N species are dominated within the N 1s spectra of SAs-Fe/N-CNSs-2, which can increase the current density and facilitate the 4-electron catalytic pathway for ORRs, respectively.[62–64] As revealed by the high-resolution Fe 2p spectra, the largest Fe–N percentage of SAs-Fe/N-CNSs-2 among the SAs-Fe/N-CNSs-*x* catalysts further manifests the existence of the highest density of Fe–N_x moieties within SAs-Fe/N-CNSs-2 (Fig. S8†). Additionally, the satellite peaks at 718.6 eV for the SAs-Fe/N-CNSs-*x* catalysts indicate the coexistence of ferrous and ferric valences in these catalysts (Fig. S8†).[65–67] Moreover, the inductively coupled plasma optical emission spectrometry (ICP-OES) measurements unveil that SAs-Fe/N-CNSs-2 possesses the highest Fe content of 2.19 wt% among the SAs-Fe/N-CNSs-*x* samples, which results from the largest amount of residual Fe–N_x species after the removal of Fe particles by acid washing (Table S2†).

To get a deeper comprehension about the local coordination structure and valency of Fe species in SAs-Fe/CNSs, X-ray absorption fine structure (XAFS) tests for SAs-Fe/N-CNSs and reference samples ($Fe_2O_3$and Fe foil) were conducted. As displayed in Fe K-edge X-ray absorption near-edge structure (XANES) spectra, the absorption edge of SAs-Fe/N-CNSs is located between those of Fe foil and Fe_2O_3 and is closer to the latter, corroborating the positive valency of Fe species among SAs-Fe/N-CNSs (Fig. 2c).[68] The positively charged Fe element in SAs-Fe/N-CNSs might result from the electron transport of Fe atoms to the adjacent nitrogen atoms (forming Fe–N_x moieties).[69] Notably, the presence of a pre-edge peak of 7114.6 eV is in accordance with the reported FePc, verifying the existence of the Fe–N_4 planar structure in SAs-Fe/N-CNSs.[70,71] Furthermore, the Fourier transform (FT) k^3-weighted Fe K-edge extended X-ray absorption fine structure (EXAFS) spectra for the samples are displayed in Fig. 2d. As expected, the predominant peak of 1.5 Å attributed to Fe–N configuration is presented in SAs-Fe/N-CNSs, proving that the iron moieties are mainly dispersed as single-atom states and coordinated with neighboring nitrogen atoms within the carbon substrate of SAs-Fe/N-CNSs.[72,73] Integrating the XRD, AC HAADF-STEM, XPS, ICP-OES, and XAFS results, we would deduce that the Fe elements are evenly dispersed within N-doped carbon substrates of SAs-Fe/N-CNSs in the form of monatomic Fe–N_x coordination structure with high density.

Subsequently, the defect degree of the carbon structure for the resulting materials was explored *via* analyzing Raman spectroscopy. As Fig. 2e and S9† reveal, all these samples exhibit two dominating peaks of approximately 1350 cm^{-1} and 1590 cm^{-1}, consistent with the D band about disordered sp^3 carbon as well as the G band about graphitic sp^2 carbon, respectively, unveiling the formation of the carbon structure in these catalysts.[68,74] Remarkably, the intensity ratios of D band to G band (I_D/I_G) were deduced to be 0.91, 0.93, 0.97, and 0.92 for SAs-Fe/N-CNSs-0, SAs-Fe/N-CNSs-1, SAs-Fe/N-CNSs-2, and SAs-Fe/N-CNSs-4, respectively. The highest I_D/I_G value of SAs-Fe/N-CNSs-2 verifies that the proper amount of $ZnCl_2$ is conducive to the formation of more defects in the carbon structure, which is quite necessary for trapping metal atoms to generate sufficient active sites for boosting the ORR performance.[75–77]

Besides the morphology, chemical composition, and carbon configuration, the specific surface area and porous characteristics for these samples are other significant factors affecting

ORR behavior, which are investigated through N_2 adsorption–desorption experiments. As demonstrated in Fig. 2f and Table S3,† the SAs-Fe/N-CNS (also named SAs-Fe/N-CNSs-2) catalyst possesses the highest Brunauer–Emmett–Teller (BET) surface area and total pore volume of 1060.80 $m^2\ g^{-1}$ and 0.73 $cm^3\ g^{-1}$, respectively, compared with SAs-Fe/N-CNSs-0 (397.56 $m^2\ g^{-1}$ and 0.24 $cm^3\ g^{-1}$), SAs-Fe/N-CNSs-1 (435.36 $m^2\ g^{-1}$ and 0.25 $cm^3\ g^{-1}$), and SAs-Fe/N-CNSs-4 (537.49 $m^2\ g^{-1}$ and 0.37 $cm^3\ g^{-1}$). Meanwhile, the characteristic type-IV curve containing a conspicuous hysteresis loop for SAs-Fe/N-CNSs corroborates its hierarchical micro/mesopore structure, which would be validated through the corresponding pore size distribution analysis in Fig. S10.†[78,79] Moreover, in contrast to NPs-Fe/N-CNSs, the SAs-Fe/N-CNS catalyst exhibits a higher BET surface area, derived from the removal of Fe-related aggregations *via* an acid washing procedure (Fig. S11 and Table S3†). Remarkably, the highest specific surface area of SAs-Fe/N-CNSs-2 among the SAs-Fe/N-CNSs-*x* catalysts is mainly attributed to its optimum $ZnCl_2$ content making for the optimal porous structure, which could be explained in detail as follows.[80] As the proportion of $ZnCl_2$ rises, more small pores would be generated from the volatilization of Zn during pyrolysis. Nevertheless, with excessive amounts of $ZnCl_2$, the Zn atoms themselves would be aggregated. Hence, a few pores in larger size would be left after the volatilization of bulk Zn-related agglomeration, which would lead to the collapse of the carbon matrix and smaller BET surface area. These results testify that self-sacrificial $ZnCl_2$ serves as a pore-forming agent to produce plenty of hierarchical micro/mesopore channels and a large BET surface area.

From the above-mentioned analyses, the hierarchical porous structure with high density of Fe–N_x moieties in SAs-Fe/N-CNSs primarily stems from the optimum molar ratio of Zn/Fe precursors, which can be further concluded in the schematic diagram in Fig. 3. With a low Zn/Fe ratio, only fewer pores can be generated within the carbon substrate, causing a lower surface area and fewer structural defects to anchor the Fe atoms. Moreover, the Fe atoms cannot be separated effectively by small quantities of Zn atoms, resulting in bulk Fe aggregations and lower density of Fe–N_x species after acid washing of Fe-relevant particles. With higher Zn/Fe ratios, the extra Zn atoms would aggregate into bulk Zn particles, which would leave fewer larger pores after the Zn volatilization, further leading to the collapse of the nanostructure, smaller BET surface area, and fewer structural defects. Besides, numerous Fe atoms neighboring the bulk Zn particles would fall off the carbon matrix accompanied by the Zn volatilization, losing plenty of highly active Fe–N_x moieties. Therefore, the optimal catalyst (SAs-Fe/N-CNSs-2) will be acquired by regulating the molar ratio of Zn/Fe precursors to 2/1 for the favorable porous structure, large BET as well as maximum density of Fe–N_x species, leading to incremental active sites and fast reactant/product transport to boost the ORR performance, which can be subsequently attested by the electrochemical tests.

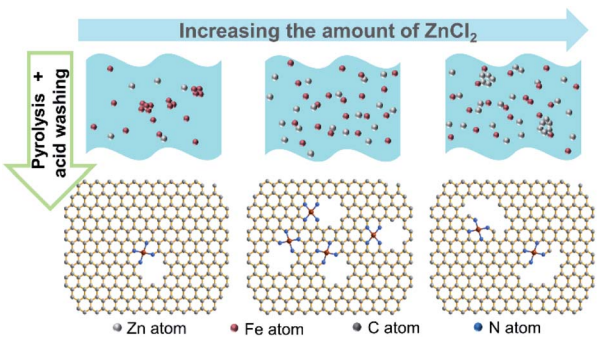

Fig. 3 Diagrammatical presentation of the influence of initial Zn/Fe molar ratio on the obtained catalysts.

We initially performed cyclic voltammetry (CV) experiments for assessing the ORR performance of SAs-Fe/N-CNSs under Ar- and O_2-saturated 0.1 M KOH media. As indicated by Fig. 4a, compared with merely indistinctive CV curve observed within an Ar-saturated electrolyte, a distinct ORR cathode peak is present in the O_2-saturated solution for SAs-Fe/N-CNSs. In addition, the SAs-Fe/N-CNSs possess the most positive cathodic peak of 0.87 V in comparison to NPs-Fe/N-CNSs (0.85 V) and N-CNSs (0.83 V) (Fig. S12†), indicative of its optimal ORR activity, which is further evidenced *via* staircase voltammetry (SCV) curves recorded on a rotating disk electrode (RDE). Fig. 4b displays that the target SAs-Fe/N-CNS (also named SAs-Fe/N-CNSs-2) catalyst exhibits more satisfactory ORR activity including onset potential (E_{onset} = 1.071 V) and half-wave potential ($E_{1/2}$ = 0.91 V) than SAs-Fe/N-CNSs-0, SAs-Fe/N-CNSs-1, and SAs-Fe/N-CNSs-4, even outperforming commercial Pt/C (E_{onset} = 1.042 V, $E_{1/2}$ = 0.896 V) together with most Fe–N–C catalysts recorded (Table S4†). The highest ORR activity of SAs-Fe/N-CNSs principally benefits from its maximum Fe–N_x density, optimal porous structure, and largest surface area, mostly resulting from the significant role of $ZnCl_2$ on spatially isolating the Fe atoms and serving as pore-forming agents. Although NPs-Fe/N-CNSs possess higher Fe and N contents, it displays much worse ORR activity than SAs-Fe/N-CNSs, confirming that the atomically dispersed Fe–N_x species are more active towards ORRs compared with Fe-related nanoparticles (Fig. S13†). Moreover, the superior ORR activity of SAs-Fe/N-CNSs to N-CNSs also reveals the promoting effect of Fe doping on ORRs (Fig. S13†). Notably, the SAs-Fe/N-CNS catalyst renders an optimized ORR activity as well, surpassing that of Co- and Ni-based single-atom catalysts acquired *via* the same synthesis procedure, which further verifies the superiority of Fe–N_x moieties (Fig. S14†). Furthermore, the kinetic current density at 0.85 V (J_k @ 0.85 V) for SAs-Fe/N-CNSs was calculated to be 29.64 mA cm^{-2}, which is 1.54, 5.36, 2.25, 2.05, 4.26, and 4.91 times of Pt/C, SAs-Fe/N-CNSs-0, SAs-Fe/N-CNSs-1, SAs-Fe/N-CNSs-4, NPs-Fe/N-CNSs, and N-CNSs, respectively, elucidating the fast reaction kinetics of SAs-Fe/N-CNSs towards the ORR process in alkaline media (Fig. 4c and S15†).

To unveil the ORR mechanism and pathway for these catalysts deeply, hydrogen peroxide yield (H_2O_2%) and electron-transfer number (n) were examined by a rotating ring-disk electrode (RRDE) method. Fig. 4d demonstrates that SAs-Fe/N-CNSs possess a calculated n value of about 3.95, approaching the Pt/C catalyst, which illustrates the dominating four-electron catalytic pathway towards ORRs. Moreover, the similarly low

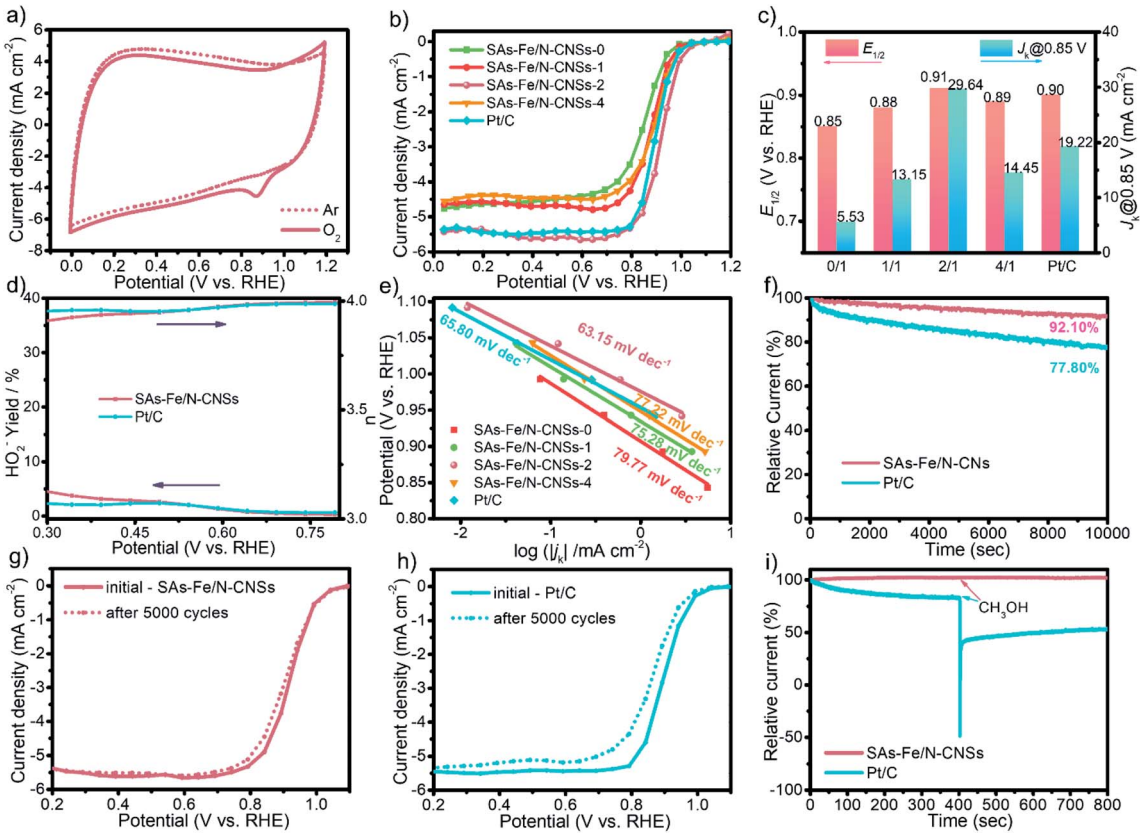

Fig. 4 (a) CV results of SAs-Fe/N-CNSs within Ar-/O_2-saturated 0.1 M KOH. (b) SCV results including SAs-Fe/N-CNSs-*x* and Pt/C under O_2-saturated 0.1 M KOH at 1600 rpm. (c) $E_{1/2}$ together with J_k @ 0.85 V (J_k at 0.85 V) results towards these materials. The 0/1, 1/1, 2/1, and 4/1 in the title of horizontal axis represent the catalysts of SAs-Fe/N-CNSs-*x* (*x* = 0, 1, 2, and 4, respectively). (d) H_2O_2 yield and electron-transport number (*n*) towards SAs-Fe/N-CNSs and Pt/C. (e) Tafel plot result towards the catalysts. (f) Chronoamperometric current measurements of SAs-Fe/N-CNSs and Pt/C within O_2-saturated 0.1 M KOH (1600 rpm, 0.793 V). SCV curves about (g) SAs-Fe/N-CNSs and (h) Pt/C before and after the stability tests within 0.6–1.0 V for 5000 cycles in an alkaline environment. (i) The i-t measurements towards SAs-Fe/N-CNSs and Pt/C with adding CH_3OH in an alkaline electrolyte at 400 s.

H_2O_2 yields of SAs-Fe/N-CNSs (below 4.3%) and Pt/C (below 2.5%) further indicate that SAs-Fe/N-CNSs tend to directly catalyze the formation of H_2O during the oxygen reduction process (Fig. 4d and S16†). By contrast, SAs-Fe/N-CNSs-0, SAs-Fe/N-CNSs-1, SAs-Fe/N-CNSs-4, NPs-Fe/N-CNSs, and N-CNSs display an obviously lower electron transfer number and higher H_2O_2 yields, owing to their inferior reaction kinetics (Fig. S17†). Additionally, the smallest Tafel slope for SAs-Fe/N-CNSs (63 mV dec^{-1}) among SAs-Fe/N-CNSs-0 (79.77 mV dec^{-1}), SAs-Fe/N-CNSs-1 (75.28 mV dec^{-1}), SAs-Fe/N-CNSs-4 (77.22 mV dec^{-1}), NPs-Fe/N-CNSs (79 mV dec^{-1}), N-CNSs (87 mV dec^{-1}), and even Pt/C (66 mV dec^{-1}) simultaneously reveals the high-efficiency kinetics towards oxygen reduction catalyzed by the SAs-Fe/N-CNSs catalyst (Fig. 4e and S18†). Electrochemical impedance spectroscopy (EIS) was performed to further unveil the interface process and kinetics of the oxygen reduction reaction. Fig. S19† shows the corresponding Nyquist plots of SAs-Fe/N-CNSs and Pt/C with semicircles in the high frequency range and inclined lines in the low frequency range, relevant to the charge transfer kinetics and diffusion-controlled process of ORRs at the electrolyte/electrode interface, respectively.[65] The smaller semicircle diameter of SAs-Fe/N-CNSs than that of Pt/C indicates that the SAs-Fe/N-CNSs enable faster charge transfer kinetics at the electrode/electrolyte interface due to its dense and efficient active sites.[81] Notably, the steeper inclined line for SAs-Fe/N-CNSs in the low frequency range verifies the superior diffusivity at the reaction interface, resulting from its optimal porous structure.[82] To sum up, the obtained SAs-Fe/N-CNSs render favorable ORR characteristics with superior reaction kinetics and high selectivity towards the four-electron pathway.

Considering the practical application of SAs-Fe/N-CNSs in electrochemical devices, the stability of the catalysts is another critical factor affecting the ORR performance, which was first examined by chronoamperometric response *i-t* tests. As displayed in Fig. 4f, SAs-Fe/N-CNSs hold 92.10% retention of the original current density, considerably exceeding commercial Pt/C (77.80% retention) after the 10 000 s operation, signifying the outstanding durability of SAs-Fe/N-CNSs during the ORR process, which was further proved *via* the accelerated durability test (ADT) under 0.1 M KOH condition. The SAs-Fe/N-CNS material (10 mV, Fig. 4g) presents ignorable variation of SCV curves before and after the 5000 cycles within 0.6–1.0 V, compared with the visibly negative $E_{1/2}$ shift of Pt/C (32 mV,

Fig. 4h). As displayed in Fig. S20,† the structure remains almost unchanged and the bright dots relevant to single Fe atoms are still uniformly scattered without Fe-related aggregation in the SAs-Fe/N-CNSs after durability tests, verifying the excellent stability of the nanostructure and Fe single atoms for SAs-Fe/N-CNSs. Besides long-term stability, methanol resistance ability is equally important for gaining desirable ORR electrocatalysts with application prospects. Fig. 4i shows that SAs-Fe/N-CNSs exhibit nearly unchanged current density in chronoamperometric tests after injecting methanol, whereas the Pt/C catalyst suffers tremendous current density degradation, implying the preferable methanol tolerance of SAs-Fe/N-CNSs. The above conclusion was further confirmed through CV and SCV measurements with methanol addition, in which an obvious methanol oxidation peak emerges in Pt/C compared with the negligible change for SAs-Fe/N-CNSs (Fig. S21†). Noticeably, the SAs-Fe/N-CNSs also possess prominent ORR performance in acidic solutions in terms of comparable half-wave potentials (0.801 V) to commercial Pt/C ($E_{1/2}$ = 0.847 V, Fig. S22†). Compared with commercial Pt/C, equally outstanding catalytic reaction kinetics in terms of the Tafel slope, H_2O_2 yield and electron transfer number together with superior methanol resistance ability are acquired for SAs-Fe/N-CNSs as revealed in Fig. S23–S25,† reflecting the desired acidic ORR performance of SAs-Fe/N-CNSs.

Taken together, the extraordinary ORR performance of SAs-Fe/N-CNSs is principally derived from its densely atomic Fe–N_x species as well as appropriate morphology and porous structure, as elaborated in detail. First, Fe–N_x moieties intrinsically act as efficient active sites availing the absorption of O_2 and the following cleavage of the O=O bond during the ORR process. Furthermore, the catalytic efficiency improves with the increase in atomic Fe–N_x densities, due to the maximum atomic efficiency and optimal electronic configuration of single atoms. Besides, the special 2D morphology contributes to the large surface area, abundant surface defects, controllable porous structure, and fluent mass/electron transfer channel for ORR. Last but not least, the SAs-Fe/N-CNS catalyst possesses hierarchical porous property including micropores and mesopores, wherein micropores would support massively exposed active sites and mesopores can accelerate transportation rates of reactants/products during the oxygen reduction reaction.[49,83] The above-mentioned superiorities make the SAs-Fe/N-CNSs catalyst one of the most fascinating NPMCs for substituting the Pt/C catalyst.

Considering the splendid ORR performance for the as-prepared SAs-Fe/N-CNSs, the homemade Zn-air battery was employed to investigate its prospect for practical applicability. As illustrated in Fig. 5a, the SAs-Fe/N-CNSs catalyst and Zn plate were employed as the cathode and anode materials in the primary Zn–air battery, respectively, with a 6 M KOH solution as the electrolyte. As a comparison sample, the Pt/C-based Zn–air battery was obtained under the same condition. Fig. 5b displays that the Zn–air battery utilizing SAs-Fe/N-CNSs delivers a higher open-circuit voltage of 1.45 V in contrast to the Pt/C catalyst (1.42 V). Moreover, their discharge polarization and power density curves are displayed in Fig. 5c. The maximum power density of the SAs-Fe/N-CNS-assembled battery reaches 157.03 mW cm^{-2}, exceeding that of the Pt/C (131.52 mW cm^{-2}) and most reported Fe-based materials (Table S5†), which further

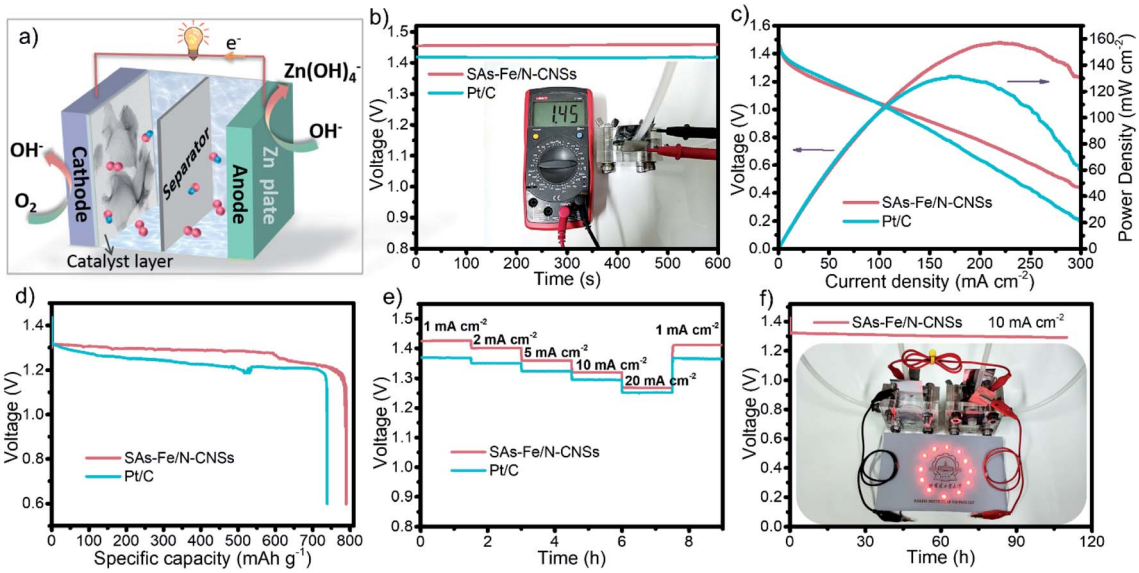

Fig. 5 (a) Schematic drawing of the primary Zn–air battery (●: OH^-, ●: O_2). (b) Open-circuit voltage result of SAs-Fe/N-CNSs and Pt/C. (The inset exhibits the photograph for the open-circuit voltage of the SAs-Fe/N-CNSs-based battery performed using a multimeter.) (c) Polarization together with power density curves towards SAs-Fe/N-CNSs- and Pt/C-assembled Zn–air batteries. (d) Specific capacity result at 10 mA cm^{-2} towards batteries utilizing SAs-Fe/N-CNSs and Pt/C as cathode materials (standardized with the mass of consumed Zn). (e) Rate capability of batteries utilizing SAs-Fe/N-CNSs and Pt/C as cathode materials. (f) Stability measurement at 10 mA cm^{-2} for batteries utilizing SAs-Fe/N-CNSs as cathode materials (recharged *via* renewing electrolyte circularly). (The inset is the photograph of red LEDs lightened through two Fe/N-CNRs-employed Zn–air batteries in series.)

reveals the superior electrochemical activity of SAs-Fe/N-CNSs. Standardized by the mass of consumed Zn in the galvanostatic discharge test at 10 mA cm^{-2}, the specific capacity and energy density of the battery with SAs-Fe/N-CNSs reached 789.82 mA h g^{-1} and 1014.91 W h kg^{-1}, respectively, superior to the commercial Pt/C (specific capacity: 738.70 mA h g^{-1}, specific energy density: 919.68 W h kg^{-1}) (Fig. 5d and S26†). By increasing the galvanostatic discharge current density (1 to 20 mA cm^{-2}), the voltage plateau in the battery utilizing SAs-Fe/N-CNSs exhibits a little drop but still locates above that of commercial Pt/C (Fig. 5e). Remarkably, the discharge voltage can be resumed with the current density reduced to 1 mA cm^{-2}, indicating the superb rate capability for our catalyst. Additionally, the stability of the air cathode catalyst is equally indispensable to popularize the application, which can be evaluated *via* the galvanostatic discharge measurement of 10 mA cm^{-2}. As Fig. 5f shows, the SAs-Fe/N-CNSs maintain a steady voltage plateau at 1.31 V for more than 100 h, verifying the outstanding discharge stability.

Furthermore, two series-wound Zn–air batteries employing SAs-Fe/N-CNSs can successfully lighten the red light-emitting diode (LED, 2.5 V) lamps, suggesting the great potential of SAs-Fe/N-CNSs as desirable cathodic catalysts for electrochemical devices (inset in Fig. 5f).

Conclusions

To sum up, we proposed a simple and versatile Zn/g-C_3N_4-mediated dual-template synthetic strategy to obtain 2D hierarchically porous single-atom Fe/N-doped carbon nanosheets (SAs-Fe/N-CNSs) featuring with high-density Fe–N_x sites, wherein g-C_3N_4 nanosheets were utilized as 2D structure guiding templates and $ZnCl_2$ acted as the self-sacrificial template to produce abundant pores. Additionally, the agglomeration of Fe atoms can be suppressed by the anchoring effect of coordinate-N holes in g-C_3N_4 as well as the spatial segregation effect of Zn atoms. Through optimizing the molar ratio of Zn/Fe to 2/1 among the precursors, atomically dispersed Fe–N_x sites with high density and uniform distribution have been acquired within the as-prepared SAs-Fe/N-CNSs, as verified by the above-mentioned XANES, EXAFS, and HAADF-STEM mapping results. Finally, the SAs-Fe/N-CNS catalyst exhibits a unique 2D morphology, large surface area, hierarchically porous structure, and densely atomic Fe–N_x moieties, which would proliferate accessible active sites and provide fluent mass/electron transport pathway for faster ORR process. As expected, the SAs-Fe/N-CNS catalyst displays better ORR performance ($E_{1/2}$ = 0.91 V) than that of Pt/C in terms of excellent activity, desirable long-term durability as well as strong toleration to toxic intermediate. It is worth noting that SAs-Fe/N-CNSs perform not only comparably to the Pt/C catalyst but superior to most published Fe-based catalysts towards ORRs in an acidic electrolyte. Furthermore, the superior Zn–air battery behavior for SAs-Fe/N-CNSs to commercial Pt/C validates the practical application potential of these prepared catalysts. This work demonstrated a feasible and cost-effective approach to achieve mass production of single-atom Fe–N–C catalysts with high Fe–N_x density for ORRs. Additionally, this strategy can be broadly applied for fabricating varieties of 2D single-atom catalysts in extensive research fields.

Author contributions

Xiao-Fei Gong performed investigation, methodology, data curation, formal analysis, visualization, writing – original draft, and writing – review & editing. Yun-Long Zhang performed investigation, formal analysis, resource collection, and writing – review & editing. Lei Zhao performed methodology, data curation, funding acquisition, resource collection, supervision, and writing – review & editing. Yun-Kun Dai performed formal analysis, resource collection, and writing – review & editing. Jia-Jun Cai performed resource collection and formal analysis. Bing Liu performed data curation and resource collection. Pan Guo performed software and resource collection. Qing-Yan Zhou performed resource collection and formal analysis. Ichizo Yagi performed resource collection, and writing – review & editing. Zhen-Bo Wang performed conceptualization, funding acquisition, resource collection, supervision, and writing – review & editing.

Conflicts of interest

There are no conflicts to declare.

Acknowledgements

We acknowledge the National Natural Science Foundation of China (Grant No. 21673064, 51802059, and 22075062), Heilongjiang Postdoctoral Fund (LBH-Z18066), and Heilongjiang Touyan Team (Grant No. HITTY-20190033).

Notes and references

1 Z. Liu, Z. Zhao, B. Peng, X. Duan and Y. Huang, *J. Am. Chem. Soc.*, 2020, **142**, 17812–17827.
2 Q. Li, R. Cao, J. Cho and G. Wu, *Adv. Energy Mater.*, 2014, **4**, 19.
3 H. Park, S. Oh, S. Lee, S. Choi and M. Oh, *Appl. Catal., B*, 2019, **246**, 322–329.
4 J. Fu, Z. P. Cano, M. G. Park, A. Yu, M. Fowler and Z. Chen, *Adv. Mater.*, 2017, **29**, 1604685.
5 C. L. Lai, M. X. Gong, Y. C. Zhou, J. Y. Fang, L. Huang, Z. P. Deng, X. P. Liu, T. H. Zhao, R. Q. Lin, K. L. Wang, K. Jiang, H. L. Xin and D. L. Wang, *Appl. Catal., B*, 2020, **274**, 119086.
6 C. Kim, F. Dionigi, V. Beermann, X. Wang, T. Moller and P. Strasser, *Adv. Mater.*, 2019, **31**, 1805617.
7 B. Liu, Y.-K. Dai, L. Li, H.-D. Zhang, L. Zhao, F.-R. Kong, X.-L. Sui and Z.-B. Wang, *Prog. Nat. Sci.: Mater. Int.*, 2020, **30**, 861–867.
8 A. Kulkarni, S. Siahrostami, A. Patel and J. K. Norskov, *Chem. Rev.*, 2018, **118**, 2302–2312.

9 L. Lv, D. C. Zha, Y. J. Ruan, Z. S. Li, X. Ao, J. Zheng, J. J. Jiang, H. M. Chen, W. H. Chiang, J. Chen and C. D. Wang, *ACS Nano*, 2018, **12**, 3042–3051.
10 H. Ji, M. Wang, S. Liu, H. Sun, J. Liu, T. Qian and C. Yan, *Energy Storage Mater.*, 2020, **27**, 226–231.
11 J. Li, A. Alsudairi, Z. F. Ma, S. Mukerjee and Q. Jia, *J. Am. Chem. Soc.*, 2017, **139**, 1384–1387.
12 D. Higgins, P. Zamani, A. Yu and Z. Chen, *Energy Environ. Sci.*, 2016, **9**, 357–390.
13 C. Domínguez, F. J. Pérez-Alonso, M. A. Salam, S. A. Al-Thabaiti, M. A. Peña, F. J. García-García, L. Barrio and S. Rojas, *Appl. Catal., B*, 2016, **183**, 185–196.
14 Z. F. Huang, J. Wang, Y. C. Peng, C. Y. Jung, A. Fisher and X. Wang, *Adv. Energy Mater.*, 2017, **7**, 21.
15 S. Dou, L. Tao, J. Huo, S. Y. Wang and L. M. Dai, *Energy Environ. Sci.*, 2016, **9**, 1320–1326.
16 H. Singh, S. Zhuang, B. Ingis, B. B. Nunna and E. S. Lee, *Carbon*, 2019, **151**, 160–174.
17 H. F. Wang, C. Tang and Q. Zhang, *Adv. Funct. Mater.*, 2018, **28**, 22.
18 I. Das, M. T. Noori, M. Shaikh, M. M. Ghangrekar and R. Ananthakrishnan, *ACS Appl. Energy Mater.*, 2020, **3**, 3512–3520.
19 Z. H. Wang, H. H. Jin, T. Meng, K. Liao, W. Q. Meng, J. L. Yang, D. P. He, Y. L. Xiong and S. C. Mu, *Adv. Funct. Mater.*, 2018, **28**, 8.
20 Y. Chen, I. Matanovic, E. Weiler, P. Atanassov and K. Artyushkova, *ACS Appl. Energy Mater.*, 2018, **1**, 5948–5953.
21 Z. L. Li, Z. C. Zhuang, F. Lv, H. Zhu, L. Zhou, M. C. Luo, J. X. Zhu, Z. Q. Lang, S. H. Feng, W. Chen, L. Q. Mai and S. J. Guo, *Adv. Mater.*, 2018, **30**, 8.
22 J. H. Kim, Y. J. Sa, H. Y. Jeong and S. H. Joo, *ACS Appl. Mater. Interfaces*, 2017, **9**, 9567–9575.
23 X. X. Wang, M. T. Swihart and G. Wu, *Nat. Catal.*, 2019, **2**, 578–589.
24 Z. Song, L. Zhang, K. Doyle-Davis, X. Fu, J.-L. Luo and X. Sun, *Adv. Energy Mater.*, 2020, **10**, 2001561.
25 B. Wang, X. Wang, J. Zou, Y. Yan, S. Xie, G. Hu, Y. Li and A. Dong, *Nano Lett.*, 2017, **17**, 2003–2009.
26 Y. Wang, H. Su, Y. He, L. Li, S. Zhu, H. Shen, P. Xie, X. Fu, G. Zhou, C. Feng, D. Zhao, F. Xiao, X. Zhu, Y. Zeng, M. Shao, S. Chen, G. Wu, J. Zeng and C. Wang, *Chem. Rev.*, 2020, **120**, 12217–12314.
27 Y. Chen, S. Ji, Y. Wang, J. Dong, W. Chen, Z. Li, R. Shen, L. Zheng, Z. Zhuang, D. Wang and Y. Li, *Angew. Chem., Int. Ed. Engl.*, 2017, **56**, 6937–6941.
28 E. F. Holby and P. Zelenay, *Nano Energy*, 2016, **29**, 54–64.
29 L. Jiao, R. Zhang, G. Wan, W. Yang, X. Wan, H. Zhou, J. Shui, S.-H. Yu and H.-L. Jiang, *Nat. Commun.*, 2020, **11**, 2831–2837.
30 H. Zhang, G. Liu, L. Shi and J. Ye, *Adv. Energy Mater.*, 2018, **8**, 1701343.
31 Y. Zhan, H. Zeng, F. Xie, H. Zhang, W. Zhang, Y. Jin, Y. Zhang, J. Chen and H. Meng, *J. Power Sources*, 2019, **431**, 31–39.
32 H. G. Zhang, H. T. Chung, D. A. Cullen, S. Wagner, U. I. Kramm, K. L. More, P. Zelenay and G. Wu, *Energy Environ. Sci.*, 2019, **12**, 2548–2558.
33 J. Wang, Z. Li, Y. Wu and Y. Li, *Adv. Mater.*, 2018, **30**, 1801649.
34 J. Wu, L. Xiong, B. Zhao, M. Liu and L. Huang, *Small Methods*, 2019, **4**, 1900540.
35 W. Lei, Y.-P. Deng, G. Li, Z. P. Cano, X. Wang, D. Luo, Y. Liu, D. Wang and Z. Chen, *ACS Catal.*, 2018, **8**, 2464–2472.
36 K. Wan, A.-d. Tan, Z.-p. Yu, Z.-x. Liang, J.-h. Piao and P. Tsiakaras, *Appl. Catal., B*, 2017, **209**, 447–454.
37 D. Liu, J.-C. Li, S. Ding, Z. Lyu, S. Feng, H. Tian, C. Huyan, M. Xu, T. Li, D. Du, P. Liu, M. Shao and Y. Lin, *Small Methods*, 2020, **4**, 1900827.
38 T. Xu, D. Yu, Z. Du, W. Huang and X. Lu, *Chem.–Eur. J.*, 2020, **26**, 10811–10816.
39 K. Yi, D. Liu, X. Chen, J. Yang, D. Wei, Y. Liu and D. Wei, *Acc. Chem. Res.*, 2021, **54**, 1011–1022.
40 J. Zhou, J. Palisaitis, J. Halim, M. Dahlqvist, Q. Tao, I. Persson, L. Hultman, P. O. Å. Persson and J. Rosen, *Science*, 2021, **373**, 801–805.
41 M. Wang, Q. Wang, W. Zhu, Y. Yang, H. Zhou, F. Zhang, L. Zhou, J. M. Razal, G. G. Wallace and J. Chen, *Green Energy Environ.*, 2017, **2**, 285–293.
42 X. Zhang, Y. Dong, F. Pan, Z. Xiang, X. Zhu and W. Lu, *Carbon*, 2021, **177**, 332–343.
43 S. Z. Butler, S. M. Hollen, L. Cao, Y. Cui, J. A. Gupta, H. R. Gutiérrez, T. F. Heinz, S. S. Hong, J. Huang, A. F. Ismach, E. Johnston-Halperin, M. Kuno, V. V. Plashnitsa, R. D. Robinson, R. S. Ruoff, S. Salahuddin, J. Shan, L. Shi, M. G. Spencer, M. Terrones, W. Windl and J. E. Goldberger, *ACS Nano*, 2013, **7**, 2898–2926.
44 Q. Deng, J. Zhao, T. Wu, G. Chen, H. A. Hansen and T. Vegge, *J. Catal.*, 2019, **370**, 378–384.
45 X. Y. Deng, X. Wang and Z. F. F. Ma, *J. Power Sources*, 2008, **183**, 604–608.
46 Z. Yang, Y. Wang, M. Zhu, Z. Li, W. Chen, W. Wei, T. Yuan, Y. Qu, Q. Xu, C. Zhao, X. Wang, P. Li, Y. Li, Y. Wu and Y. Li, *ACS Catal.*, 2019, **9**, 2158–2163.
47 L. Zheng, S. Yu, X. Lu, W. Fan, B. Chi, Y. Ye, X. Shi, J. Zeng, X. Li and S. Liao, *ACS Appl. Mater. Interfaces*, 2020, **12**, 13878–13887.
48 Y. Zhou, X. Tao, G. Chen, R. Lu, D. Wang, M. X. Chen, E. Jin, J. Yang, H. W. Liang, Y. Zhao, X. Feng, A. Narita and K. Mullen, *Nat. Commun.*, 2020, **11**, 5892.
49 D. Wang, H. Xu, P. Yang, L. Xiao, L. Du, X. Lu, R. Li, J. Zhang and M. An, *J. Mater. Chem. A*, 2021, **9**, 9761–9770.
50 R. Gokhale, Y. Chen, A. Serov, K. Artyushkova and P. Atanassov, *Electrochim. Acta*, 2017, **224**, 49–55.
51 J. Hao, Y. Wang, X. Qiu, M. Liu, W. Li and J. Li, *ACS Appl. Mater. Interfaces*, 2021, **13**, 28140–28149.
52 K. X. Wang, J. A. Zhang, W. Xia, R. Q. Zou, J. H. Guo, Z. M. Gao, W. F. Yan, S. J. Guo and Q. Xu, *J. Mater. Chem. A*, 2015, **3**, 18867–18873.
53 D. Deng, K. S. Novoselov, Q. Fu, N. Zheng, Z. Tian and X. Bao, *Nat. Nanotechnol.*, 2016, **11**, 218–230.
54 Z. Sun, J. Lin, K. Hou, L. Guan and H. Zhan, *J. Mater. Chem. A*, 2020, **8**, 7273–7279.

55 L. Zhang, J. Xiong, Y.-H. Qin and C.-W. Wang, *Carbon*, 2019, **150**, 475–484.
56 J. Han, X. Meng, L. Lu, J. Bian, Z. Li and C. Sun, *Adv. Funct. Mater.*, 2019, **29**, 1808872.
57 Y. Pan, S. Liu, K. Sun, X. Chen, B. Wang, K. Wu, X. Cao, W. C. Cheong, R. Shen, A. Han, Z. Chen, L. Zheng, J. Luo, Y. Lin, Y. Liu, D. Wang, Q. Peng, Q. Zhang, C. Chen and Y. Li, *Angew. Chem., Int. Ed. Engl.*, 2018, **57**, 8614–8618.
58 F. Xiao, G.-L. Xu, C.-J. Sun, M. Xu, W. Wen, Q. Wang, M. Gu, S. Zhu, Y. Li, Z. Wei, X. Pan, J. Wang, K. Amine and M. Shao, *Nano Energy*, 2019, **61**, 60–68.
59 L. Yang, L. Shi, D. Wang, Y. Lv and D. Cao, *Nano Energy*, 2018, **50**, 691–698.
60 R. Ding, Y. Liu, Z. Rui, J. Li, J. Liu and Z. Zou, *Nano Res.*, 2020, **13**, 1519–1526.
61 G. Wang, J. Deng, T. Yan, J. Zhang, L. Shi and D. Zhang, *Nanoscale*, 2020, **12**, 5601–5611.
62 D. Guo, R. Shibuya, C. Akiba, S. Saji, T. Kondo and J. Nakamura, *Science*, 2016, **351**, 361–365.
63 A. S. Haile, H. A. Hansen, W. Yohannes and Y. S. Mekonnen, *J. Phys. Chem. Lett.*, 2021, **12**, 3552–3559.
64 K. Mamtani, D. Jain, D. Dogu, V. Gustin, S. Gunduz, A. C. Co and U. S. Ozkan, *Appl. Catal., B*, 2018, **220**, 88–97.
65 M. Sun, D. Davenport, H. Liu, J. Qu, M. Elimelech and J. Li, *J. Mater. Chem. A*, 2018, **6**, 2527–2539.
66 Y. Yao, H. Yin, M. Gao, Y. Hu, H. Hu, M. Yu and S. Wang, *Chem. Eng. Sci.*, 2019, **209**, 115211.
67 K. Yuan, D. Lutzenkirchen-Hecht, L. Li, L. Shuai, Y. Li, R. Cao, M. Qiu, X. Zhuang, M. K. H. Leung, Y. Chen and U. Scherf, *J. Am. Chem. Soc.*, 2020, **142**, 2404–2412.
68 X. Zhang, X. Han, Z. Jiang, J. Xu, L. Chen, Y. Xue, A. Nie, Z. Xie, Q. Kuang and L. Zheng, *Nano Energy*, 2020, **71**, 104547.
69 J. Feng, M. Dou, Z. Zhang and F. Wang, *ACS Appl. Mater. Interfaces*, 2018, **10**, 37079–37086.
70 Y. Chen, Z. Li, Y. Zhu, D. Sun, X. Liu, L. Xu and Y. Tang, *Adv. Mater.*, 2019, **31**, 1806312.
71 J. Huo, L. Lu, Z. Shen, Y. Liu, J. Guo, Q. Liu, Y. Wang, H. Liu, M. Wu and G. Wang, *J. Mater. Chem. A*, 2020, **8**, 16271–16282.
72 Z. Zhang, J. Sun, F. Wang and L. Dai, *Angew. Chem., Int. Ed. Engl.*, 2018, **57**, 9038–9043.
73 L. Zhao, Y. Zhang, L. B. Huang, X. Z. Liu, Q. H. Zhang, C. He, Z. Y. Wu, L. J. Zhang, J. Wu, W. Yang, L. Gu, J. S. Hu and L. J. Wan, *Nat. Commun.*, 2019, **10**, 1278.
74 P. Chen, T. Zhou, L. Xing, K. Xu, Y. Tong, H. Xie, L. Zhang, W. Yan, W. Chu, C. Wu and Y. Xie, *Angew. Chem., Int. Ed. Engl.*, 2017, **56**, 610–614.
75 W. Li, D. D. Wang, Y. Q. Zhang, L. Tao, T. H. Wang, Y. Q. Zou, Y. Y. Wang, R. Chen and S. Y. Wang, *Adv. Mater.*, 2020, **32**, 20.
76 Y. Deng, B. Chi, X. Tian, Z. Cui, E. Liu, Q. Jia, W. Fan, G. Wang, D. Dang, M. Li, K. Zang, J. Luo, Y. Hu, S. Liao, X. Sun and S. Mukerjee, *J. Mater. Chem. A*, 2019, **7**, 5020–5030.
77 Y. Qin, J. Yi, W. Fenfei, Z. Linzhou, Y. Dongjiang, L. Jizi, W. Xin, S. Lin, Y. Pei and Y. Xiangdong, *Angew. Chem., Int. Ed.*, 2020, **132**, 6178–6183.
78 Q. Wang, Y. Yang, F. Sun, G. Chen, J. Wang, L. Peng, W. T. Chen, L. Shang, J. Zhao, D. Sun-Waterhouse, T. Zhang and G. I. N. Waterhouse, *Adv. Energy Mater.*, 2021, **11**, 2100219.
79 Y. Liu, B. Wang, Q. Sun, Q. Pan, N. Zhao, Z. Li, Y. Yang and X. Sun, *ACS Appl. Mater. Interfaces*, 2020, **12**, 16512–16520.
80 C. Zhu, Q. Shi, B. Z. Xu, S. Fu, G. Wan, C. Yang, S. Yao, J. Song, H. Zhou, D. Du, S. P. Beckman, D. Su and Y. Lin, *Adv. Energy Mater.*, 2018, **8**, 1801956.
81 G.-S. Kang, J.-H. Jang, S.-Y. Son, C.-H. Lee, Y.-K. Lee, D. C. Lee, S. J. Yoo, S. Lee and H.-I. Joh, *J. Mater. Chem. A*, 2020, **8**, 22379–22388.
82 S. Gao, B. Fan, R. Feng, C. Ye, X. Wei, J. Liu and X. Bu, *Nano Energy*, 2017, **40**, 462–470.
83 X. Xie, L. Peng, H. Yang, G. I. N. Waterhouse, L. Shang and T. Zhang, *Adv. Mater.*, 2021, **33**, 2101038.